

APPENDIX 1

Atmospheric correction of ocean color sensors: Effects of earth curvature

By

Kuiyuan Ding and Howard R. Gordon

Department of Physics

University of Miami

Coral Gables, Florida 33124

(Submitted to *Applied Optics*)

Acknowledgement

We are grateful to G. Kattawar and C. Adams for carrying out Monte Carlo computations, in addition to those presented in Ref. (16), for the validation of our spherical-shell atmosphere code, to M. Wang for providing help in testing the SeaWiFS correction algorithm with radiances computed for a spherical-shell atmosphere, and to the National Aeronautics and Space Administration for support under Grant NAGW-273 and Contracts NAS5-31363 and NAS5-31743.

Abstract

The influence of the curvature of the earth on a proposed atmospheric correction scheme for the Sea-viewing Wide Field-of-view Sensor (SeaWiFS) is investigated by simulating the radiance exiting the top of a spherical-shell atmosphere and inserting the result into the proposed correction algorithm. The error in the derived water-leaving reflectance suggests that the effects of the curvature appear to be negligible for solar zenith angles $(\theta_0) \leq 70^\circ$. Furthermore, for $\theta_0 > 70^\circ$ the error in atmospheric correction can usually be reduced by computing the molecular scattering component of the top of the atmosphere reflectance (ρ_r) using a spherical-shell atmosphere radiative transfer code. Also, for $\theta_0 > 70^\circ$ the error can be predicted reasonably well from computations made with plane-parallel atmosphere radiative transfer codes, when ρ_r is computed for a spherical-shell atmosphere. This implies that studies aimed at improving atmospheric correction can be made assuming plane-parallel geometry, and that the investigator can be confident when $\theta_0 > 70^\circ$ the results will still be valid as long as ρ_r is computed in spherical-shell geometry. Finally, a scheme is developed for computing ρ_r in a spherical-shell atmosphere in a simple manner.

Introduction

Ocean color contains information about the constituents of the ocean, because it can be related to their absorption and scattering properties. The most important constituent influencing ocean color in the open ocean is phytoplankton, microscopic plant organisms that photosynthesize the marine light field. During photosynthesis, phytoplankton take in carbon dioxide and produce carbohydrates, and thus form the primary link in the marine food chain. This production of carbohydrates is termed *primary production*. A portion of the carbon that they take up during the process will eventually reach the ocean floor, so understanding the spatial-temporal variability in the concentration of phytoplankton in the ocean will aid in the understanding of the ocean's role in the global carbon cycle. In 1978 NASA launched the Coastal Zone Color Scanner (CZCS) on the satellite Nimbus-7 to study the feasibility of measuring the phytoplankton concentration by space-based ocean color sensors.¹ The CZCS mission demonstrated that measurement of phytoplankton light-harvesting pigments,^{2,3} and possibly even primary productivity,^{4,5} could be made on a *global* scale.

Of the total signal received by an ocean color sensor at satellite altitudes, typically in the blue over 80% is from the contribution of scattering by molecules and particles (aerosols) in the atmosphere. The ocean color signal (the water-leaving radiance, L_w), from which we derive the phytoplankton concentration, is buried in the total radiance (L_t) reaching the sensor. The process of retrieving L_w from L_t is usually referred to as atmospheric correction. Gordon⁶ developed an atmospheric correction algorithm for processing the CZCS data. In most circumstances it performed reasonably well, considering the radiometric sensitivity of the CZCS instrument,⁷ and the entire global data set has been processed with it.⁸ However, future ocean color sensors, such as the Sea-viewing Wide Field-of-view Sensor (SeaWiFS)⁹ and the Moderate Resolution Imaging Spectroradiometer (MODIS),¹⁰ which are scheduled to be launched by NASA in 1994 and 1998, respectively, will possess sensitivities superior to CZCS and will require a more accurate atmospheric correction. To meet the needs of these instruments, a systematic investigation of processes that were ignored in the CZCS algorithm — the influence of multiple scattering,¹¹ the influence of polarization on the computation of the molecular scattering component,¹² and the influence of wind-induced sea surface roughness on the molecular scattering component¹³ and on atmospheric correction in general¹⁴ — was undertaken. These studies have led to a preliminary atmospheric correction algorithm for SeaWiFS;¹⁵ however, several aspects remain to be considered. For example,

in the CZCS and the proposed SeaWiFS algorithms, it is assumed that the atmosphere is a plane-parallel medium rather than the more appropriate spherical-shell medium. Adams and Kattawar¹⁶ showed that, for a very simple one-layer Rayleigh-scattering medium with a totally absorbing lower boundary, there could be significant differences between the radiance reflected from plane-parallel and spherical-shell media for large solar zenith angles. In this paper, we examine the influence of earth curvature on the proposed SeaWiFS algorithm.

We begin with the computational techniques for working out the radiative transfer problem for a spherical-shell atmosphere. Next, we apply the simulated radiances from such an atmosphere to the SeaWiFS atmospheric correction algorithm to look at the earth curvature effects on the algorithm. Finally, some practical considerations for including the earth curvature effects in the proposed SeaWiFS correction method are discussed.

Computational Procedure

The distribution and propagation of the light field in an optical medium are governed by the Radiative Transfer Equation (RTE). In general, the RTE takes the following form:

$$\hat{\xi} \cdot \nabla L(\mathbf{r}, \hat{\xi}) = -c(\mathbf{r})L(\mathbf{r}, \hat{\xi}) + \int \beta(\mathbf{r}, \hat{\xi}' \rightarrow \hat{\xi})L(\mathbf{r}, \hat{\xi}')d\Omega(\hat{\xi}') + J(\mathbf{r}, \hat{\xi})$$

where L is the radiance to be determined, c is the beam attenuation coefficient of the medium, \mathbf{r} is the position vector where the radiance L is measured, $\hat{\xi}$ is a unit vector in the direction in which the radiance is traveling, β is the volume scattering function (differential scattering cross section per unit volume) of the medium, and J represents the total contribution from any internal sources. The beam attenuation coefficient is the sum of the scattering coefficient,

$$b(\mathbf{r}) = \int \beta(\mathbf{r}, \hat{\xi}' \rightarrow \hat{\xi})d\Omega(\hat{\xi}'),$$

and the absorption coefficient $a(\mathbf{r})$.

In our study we need to solve the RTE in two geometries. The first is a plane-parallel atmosphere (PPA) in which β , c , L , and J are all invariant under translations parallel to the boundaries. In this case, the RTE simplifies considerably. The second is for a spherical-shell atmosphere (SSA) in which β and c are functions of the radius of the shell only, i.e., functions of $r = |\mathbf{r}|$. However, because the incident illumination does not have spherical symmetry, L and J still depend on \mathbf{r} .

We have chosen a Monte Carlo procedure to solve the RTE in spherical geometry. There are basically four major steps in the Monte Carlo procedure. First, a photon is sent into the medium in the same direction as the solar beam; second, the distance the photon will travel before being absorbed or scattered in the medium is determined from random sampling based on the beam attenuation coefficient of the medium; third, at the point of interaction, the contribution of the photon to the radiance (the estimator) at a particular point due to this interaction is calculated and collected; and forth, the new direction that the photon will travel in the medium is generated by sampling the phase function ($P = \beta/b$). This process is repeated until the photon exits the medium, and then a new photon is initiated. Because L depends on the absolute position of the detector in the medium, we have chosen to solve the RTE using a *Backward* Monte Carlo (BMC) technique as used by Collins et al.,¹⁷ Adams and Kattawar,¹⁶ and Gordon.¹⁸ This is more efficient for determining radiometric quantities at a point. The BMC works the same as the normal Monte Carlo except that positions of the source (the sun) and the receiver (the sensor) are interchanged, i.e., photons are started from the detector and traced through the medium. At the i^{th} interaction point in the medium the probability that the photon will be scattered in the direction of the sun is recorded. This is $(\omega_0 PT)_i$, where $\omega_0 = b/c$, P is the phase function for scattering from the photon's direction of propagation to the sun, and T is the atmospheric transmittance from the interaction point to the sun. The photon is then allowed to scatter and the process continues until the photon leaves the medium. The radiance at the detector is just

$$L = \frac{F_0 \sum_i (\omega_0 PT)_i}{N},$$

where F_0 is the incident extraterrestrial solar irradiance, N is the total number of photons used in the simulation, and the sum is the accumulation of the estimator collected at each interaction.

Figure 1 describes the geometry of the RTE problem of the SSA model. The z -axis of the coordinate system points to the sensor position from the origin (the center of the earth); the x -axis is the projection of the solar beam direction on the plane perpendicular to the z -axis; and the y -axis is then determined by the right-hand rule. The atmosphere is assumed to be a two-layer medium: the Rayleigh-scattering molecules are in the upper layer (18 km thick); and the aerosols, small particles suspended in the air, which typically scatter very strongly in the forward direction, are in the lower layer (2 km thick). The Fresnel-reflecting ocean surface is the inner boundary of the atmosphere. As in the real remote sensing situation, the satellite sensor is located at a height of 705 km above the earth surface. Of course, all of the geometrical quantities are adjustable parameters

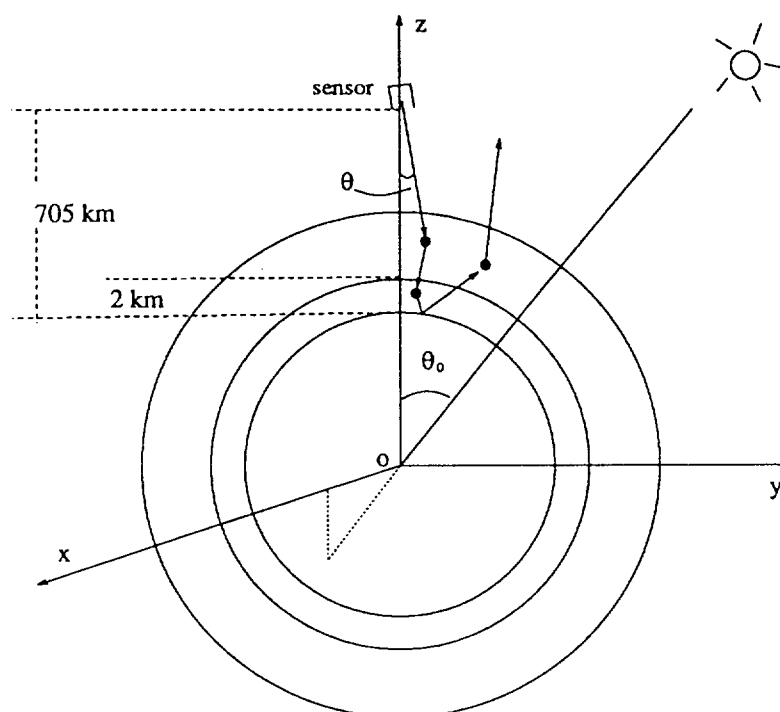


Figure 1. The geometry of the radiative transfer problem for the SSA model.

in the code for the computation. As the Monte Carlo procedure is backward, the photon will be injected into the medium from the sensor position in the viewing direction (θ, ϕ) , where ϕ is not drawn in the diagram. Then it will be followed throughout its journey in the atmosphere. Special attention must be paid to the interface of the upper and lower layers of the atmosphere in the determination of the free-travelling path of the photon.

When the photon hits the sea surface, it will be reflected. For a smooth ocean surface, the new direction after the reflection can be decided simply from Fresnel's laws of reflection. For the contribution to the radiance, when the Fresnel-reflecting surface is included, there are two paths that the photon can take toward the Sun at each point of interaction in the atmosphere. The photon can be scattered into the Sun's direction, or it can also be first scattered toward the ocean surface and then reflected toward the Sun (Figure 2). A difficulty for the evaluation for the contribution of the second part is the determination of the proper position on the ocean surface at which the photon has to reflect in order to be directed toward the Sun. For a smooth ocean surface this turns out to be governed by a non-linear equation involving the related angles and distances. This equation was solved by iteration, with convergence usually achieved in two or three steps.¹⁹

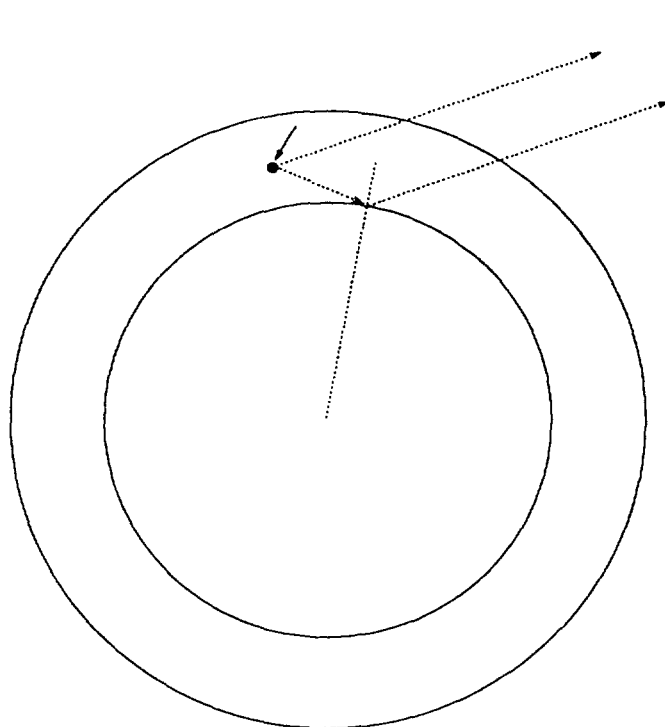


Figure 2. An example of the two contributions to the radiance in the presence of a Fresnel-reflecting sea surface.

The code that executes the BMC procedure has been tested extensively. For a one-layer Rayleigh-scattering medium with a totally absorbing ocean surface radiances generated were found to agree very well (differences $\lesssim 0.3\%$) with computations of Adams and Kattawar¹⁶ for the same conditions. Also comparisons were made to the PPA results calculated using the successive order of scattering method^{13,14,20} for several situations. It was found that the SSA computations satisfactorily approached the PPA radiances as the radius of the earth was increased to very large values. We have also included a wind-roughened Fresnel-reflecting ocean surface obeying the Cox and Munk²¹ slope distribution in the SSA model; however, the special techniques developed to deal with roughness will not be described here, because only a smooth surface is considered.

Curvature effects on SeaWiFS atmospheric correction

The radiometric specifications of the SeaWiFS instrument are provided and compared with the CZCS in Table 1. The various quantities are given in reflectance units, where a reflectance ρ

associated with a radiance L is defined to be $\pi L/F_0 \cos \theta_0$. ρ_{max} is the saturation reflectance,

Table 1: Comparison of the radiometric performance of SeaWiFS, and CZCS for $\theta_0 = 60^\circ$ near the scan edge.

Band	λ (nm)	ρ_{max} (sr ⁻¹)	ρ_t (sr ⁻¹)	ρ_w (sr ⁻¹)	NE $\Delta\rho$ (sr ⁻¹)	
					SeaWiFS	CZCS
1	402–422	0.50	0.34	0.040	0.00068	–
2	433–453	0.46	0.29	0.038	0.00043	0.0011
3	480–500	0.36	0.23	0.024	0.00034	–
4	500–520	0.30	0.19	0.0090	0.00031	0.00058
5	545–565	0.25	0.154	0.0040	0.00027	0.00064
6	660–680	0.17	0.105	0.0004	0.00023	0.00051
7	745–785	0.15	0.081	–	0.00018	–
8	845–885	0.13	0.069	–	0.00015	–

ρ_t is a typical value for the reflectance at the top of the atmosphere, and ρ_w is the water-leaving reflectance (at the sea surface) for very clear ocean water, e.g., the Sargasso Sea in summer. NE $\Delta\rho$ is the “noise equivalent reflectance,” and λ is wavelength. Since the SeaWiFS radiometric sensitivity will be superior to that of the CZCS, through a lower NE $\Delta\rho$ (Table 1) and the adoption of smaller quantization increment (10-bit as opposed to 8-bit), the requirement for the atmospheric correction accuracy accordingly will be higher. The goal of the SeaWiFS correction is to recover the water-leaving reflectance ρ_w with no more than 5% error in the blue. At 443 nm, ρ_w is about 0.02–0.04 for clear water, which implies that the error $\Delta\rho_w(443)$ should be $\leq 0.001 - 0.002$.

The total signal received by a satellite ocean sensor is composed of several parts, i.e.,

$$\rho_t(\lambda) = \rho_r(\lambda) + \rho_a(\lambda) + \rho_{ra}(\lambda) + t\rho_w(\lambda), \quad (1)$$

where ρ_r is the contribution from Rayleigh scattering, ρ_a is the contribution from aerosol scattering, ρ_{ra} represents the interaction of Rayleigh and aerosol scattering, and ρ_w is the desired water-leaving radiance (t is the diffuse transmittance from the ocean surface to the sensor). In our study of the earth curvature effects here, the reflectances are computed by solving the radiative transfer equation using the SSA model. This provides simulated values of ρ_t that include the effects of the earth’s curvature. These simulated radiances are then inserted into the atmospheric correction algorithm and $t\rho_w$ is derived. The error $\Delta\rho \equiv t\Delta\rho_w$ was then computed.

We examined the atmospheric correction algorithm proposed for SeaWiFS by Gordon and Wang.¹⁵ Briefly, the increased sensitivity of SeaWiFS over CZCS requires the consideration of multiple scattering in the atmosphere. Through simulations using the PPA approximation they¹⁵ found that the effects of multiple scattering are dependent on the model used to describe the aerosol scattering. Thus, in their scheme, aerosol models are employed to include the multiple scattering effects. The appropriate model is chosen from several candidates based on the variation of $\rho_t - \rho_r$ between bands 7 and 8, in which ρ_w can be taken to be zero. The candidate aerosol models were taken from those developed by Shettle and Fenn²² for LOWTRAN-6.²³ In particular, Gordon and Wang used the Maritime and Tropospheric models, and introduced a Coastal model containing half the fraction of the sea salt aerosol that was in the Maritime model. The Coastal model simulates situations that may be expected to occur near the coast (larger continental influence). With the resulting size distributions and refractive indices, Mie theory was used to compute the aerosol optical properties for the SeaWiFS bands as a function of the relative humidity (RH). Three values of RH (70%, 90%, and 98%) were used for each of the three models (Maritime, Coastal, and Tropospheric) for a total of nine candidate models. When tested using ρ_t computed with the Maritime, Coastal, and Tropospheric models with RH = 80% (*not* among the candidate models), Gordon and Wang found that the resulting $\Delta\rho$ was usually in the right range, i.e., $\lesssim 0.001 - 0.002$.

Since the Gordon and Wang algorithm was developed for a PPA, it is important to understand its performance in the more realistic spherical-shell atmosphere. Thus, we used the SSA code to simulate ρ_t for each aerosol model that Gordon and Wang used to test the algorithm. The aerosol optical thickness at 865, $\tau_a(865)$, was taken to be 0.2. This is about twice the value of τ_a at 800 nm over the North Atlantic in situations where air mass trajectory analysis suggests a presence of only a maritime aerosol.²⁴ The resulting ρ_t was then used as input into an implementation of the correction algorithm utilizing twelve candidate models, and the error in correction $\Delta\rho$ was computed at the center of the SeaWiFS scan (nadir viewing) and at the edge of the scan (θ in Figure 1 was $\sim 45^\circ$ and in the y - z plane). The results of this exercise are presented in Figure 3. For each panel of Figure 3 there are three sets of curves. The filled circles provide the error estimation as a function of θ_0 when ρ_t is simulated using the PPA, i.e., the results originally presented by Gordon and Wang¹⁵ in which the PPA-developed algorithm is tested using PPA-generated pseudodata. The filled squares provide the error when the SSA-generated ρ_t is used in the algorithm. In this case the PPA is used to compute ρ_r . [Recall that the spectral variation of $\rho_t - \rho_r$ in the near infrared

is used in the algorithm to select an aerosol model from the candidate models, and that 443 nm ρ_r must be subtracted from ρ_t in the derivation of $t\rho_w(443)$ (Eq. (1)).]

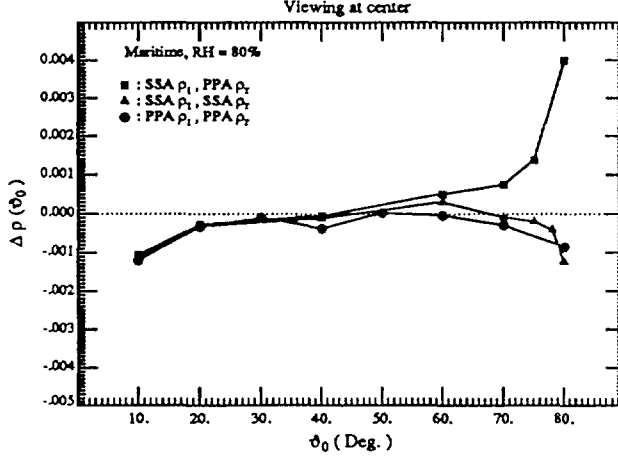


Figure 3a. Error in atmospheric correction at 443 nm at the scan center for the Maritime aerosol model, with $\tau_a(865) = 0.2$.

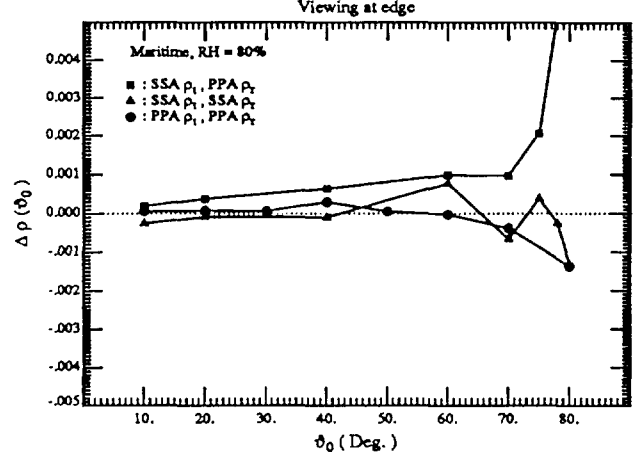


Figure 3b. Error in atmospheric correction at 443 nm at the scan edge for the Maritime aerosol model, with $\tau_a(865) = 0.2$.

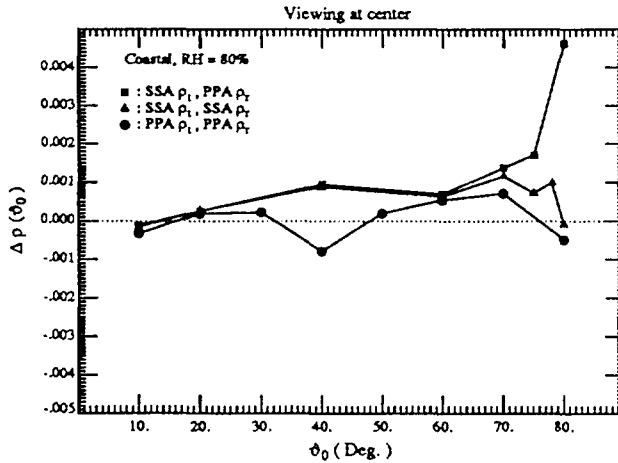


Figure 3c. Error in atmospheric correction at 443 nm at the scan center for the Coastal aerosol model, with $\tau_a(865) = 0.2$.

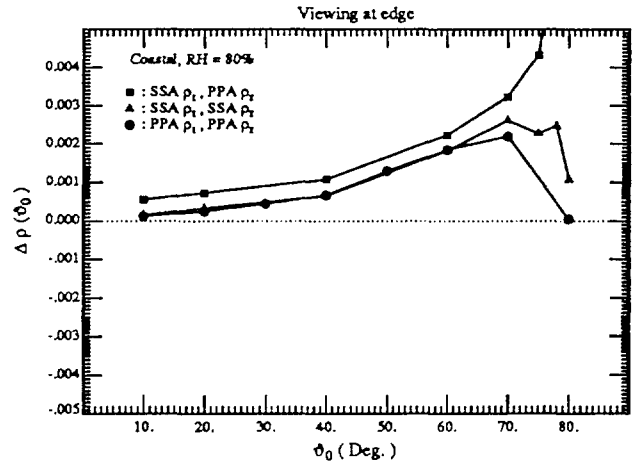


Figure 3d. Error in atmospheric correction at 443 nm at the scan edge for the Coastal aerosol model, with $\tau_a(865) = 0.2$.

The filled triangles provide the error when ρ_r is computed using the SSA. The figure shows that the PPA algorithm works well with SSA pseudodata for $\theta_0 \lesssim 70^\circ$; however, for $\theta_0 \gtrsim 70^\circ$ there can be very large errors. In contrast, when ρ_r is computed using the SSA model (filled triangles), the

algorithm provides essentially the same error pattern as when both ρ_t and ρ_r are computed using

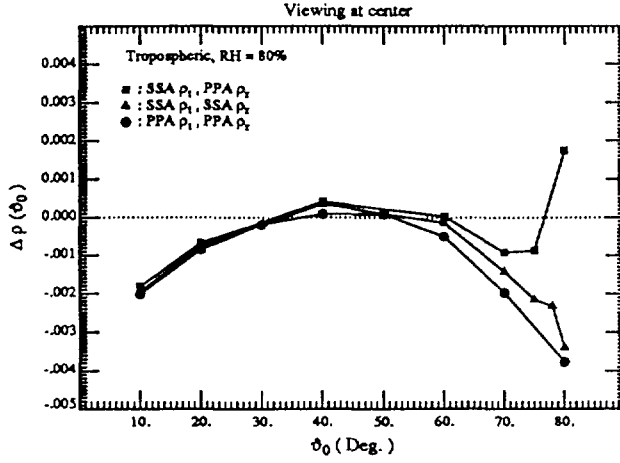


Figure 3e. Error in atmospheric correction at 443 nm at the scan center for the Tropospheric aerosol model, with $\tau_a(865) = 0.2$.

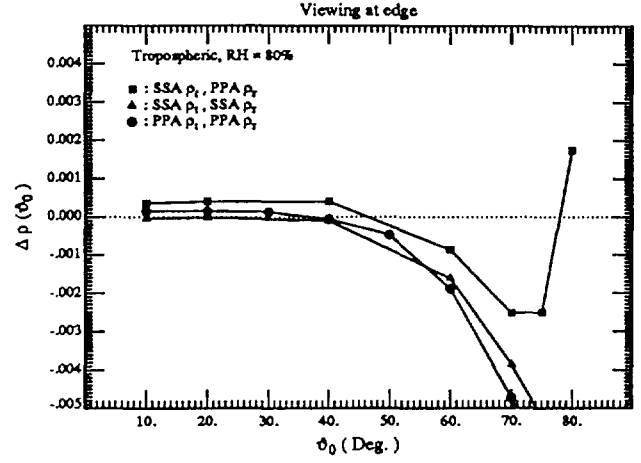


Figure 3f. Error in atmospheric correction at 443 nm at the scan edge for the Tropospheric aerosol model, with $\tau_a(865) = 0.2$.

the PPA model. In other words, as long as ρ_r is computed using a SSA model, the algorithm should perform in a realistic atmosphere in a manner *quantitatively* similar to its performance in the PPA model. This is important because it suggests that research toward improving the algorithm can be carried out using the less costly PPA radiative transfer codes.

We also carried out similar simulations to assess the effect of the earth's curvature on the performance of the original CZCS correction algorithm. Owing to the fact that the original algorithm did not satisfactorily address multiple scattering, its inherent accuracy is less than the SeaWiFS algorithm, and we found that neglecting earth curvature often actually *improved* the performance of the algorithm somewhat for $\theta_0 \geq 70^\circ$. Thus, there appears to be no necessity to reprocess high-latitude CZCS imagery with an algorithm in which earth-curvature effects are incorporated into the computation of ρ_r .

Calculation of the Rayleigh Scattering

In the previous section we have seen that for the SeaWiFS atmospheric correction scheme the Rayleigh scattering component must be calculated using the SSA model in order to achieve satisfactory accuracy at large solar zenith angles ($\theta_0 \geq 70^\circ$). For the results presented in Figures 3a through 3f this calculation was done through the Monte Carlo simulation technique, which is

very computation intensive and, therefore, impractical for the processing of ocean color imagery, or for the preparation of lookup tables for the Rayleigh scattering component. Thus, we have tried to develop an alternative approach.

Our approach is based on the observation of Adams and Kattawar¹⁶ that the ratio of single scattering radiance to total radiance is nearly the same for a PPA and a SSA model under same conditions. That is, if we write the total radiance as $T = S + M$, where S and M are the single and multiple scattering components, and use the subscripts PPA and SSA to indicate a PPA and SSA model, respectively, they found that

$$\frac{S_{SSA}}{T_{SSA}} \approx \frac{S_{PPA}}{T_{PPA}} \quad (2)$$

for the same optical thickness, viewing direction and solar zenith angle. This is useful because an analytical expression can be written to compute the single scattering part of the total SSA Rayleigh radiance. (Note, however, it still must be evaluated numerically.) Based on the reciprocity principle²⁵ we were able to calculate this component for the case of a smooth ocean surface at the bottom of the spherical-shell atmosphere. Our results were extensively compared to Monte Carlo simulations under the same conditions and excellent agreement was obtained. Adams and Kattawar tested only cases with $\tau_r = 0.25$ and 1.0 , where here and hereafter τ_r is the optical thickness of the Rayleigh-scattering molecules. We examined the conjecture [Eq. (2)] for smaller optical thicknesses, i.e., the case of the longer-wave SeaWiFS bands, and found that the two ratios differed by $\sim 2\%$. This would be a significant error in the SeaWiFS correction algorithm. However, we also observed that for the same viewing direction and optical thickness, the ratio of the multiple scattering radiance for the SSA model (M_{SSA}) to that for the PPA model (M_{PPA}) remains nearly constant for different solar zenith angles (θ_0), i.e.,

$$\alpha \equiv \frac{M_{SSA}}{M_{PPA}} \quad (3)$$

is nearly independent of θ_0 . This is shown in Figures 4a through 4d. However, α is a function of the viewing angle θ for a fixed solar zenith angle. This is demonstrated in Figure 5 for $\theta_0 = 40^\circ$ and for several SeaWiFS bands. Note that for a fixed θ_0 , α changes very smoothly with viewing angles.

From these observations, we developed the following empirical scheme for deriving the total scattering radiance for the SSA model from the PPA computations. First, for different wavelengths,

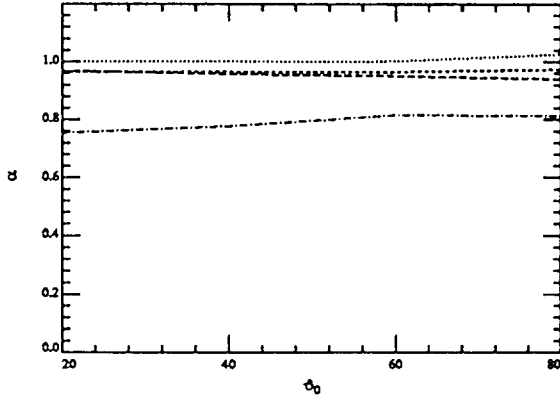


Figure 4a. At $\theta = 5^\circ$ ($\phi = 90^\circ$) M_{ssa}/M_{ppa} changes very slowly with respect to θ_0 for different SeaWiFS bands. The curves from top to bottom refer to $\lambda = 412, 550, 670$ and 865 nm.

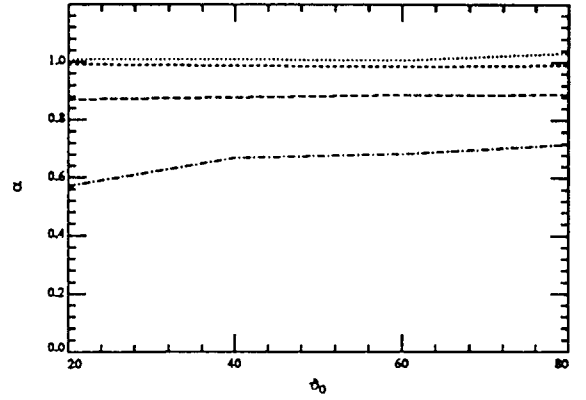


Figure 4b. At $\theta = 20^\circ$ ($\phi = 90^\circ$) M_{ssa}/M_{ppa} changes very slowly with respect to θ_0 for different SeaWiFS bands. The curves from top to bottom refer to $\lambda = 412, 550, 670$ and 865 nm.

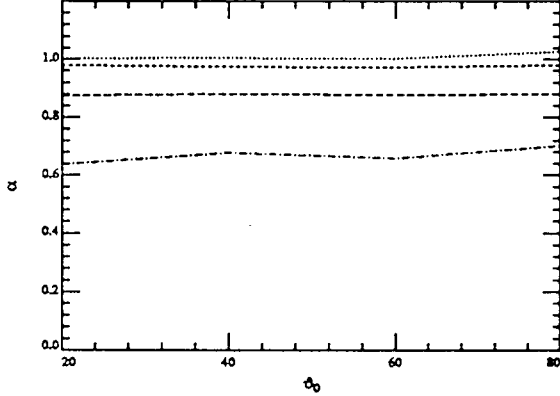


Figure 4c. At $\theta = 40^\circ$ ($\phi = 90^\circ$) M_{ssa}/M_{ppa} changes very slowly with respect to θ_0 for different SeaWiFS bands. The curves from top to bottom refer to $\lambda = 412, 550, 670$ and 865 nm.

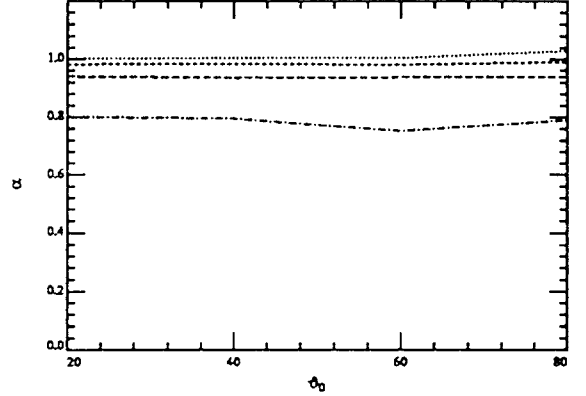


Figure 4d. At $\theta = 60^\circ$ ($\phi = 90^\circ$) M_{ssa}/M_{ppa} changes very slowly with respect to θ_0 for different SeaWiFS bands. The curves from top to bottom refer to $\lambda = 412, 550, 670$ and 865 nm.

i.e., τ_r 's, we compute the SSA total radiance "exactly" using Monte Carlo simulation for one solar zenith angle, e.g., $\theta_0 = 40^\circ$, and for several viewing directions to estimate the α 's. The α 's

obtained in this manner are then used for all other solar zenith angles, and if we knew M_{SSA} , we could combine it with S_{SSA} to obtain T_{SSA} . Formally, we let

$$\beta \equiv \frac{M_{SSA}}{T_{SSA}} = \frac{\alpha M_{PPA}}{T_{SSA}}$$

and note that since multiple scattering is usually quite small throughout the visible, a small error in β will not be significant. Thus we approximate β by

$$\beta \approx \frac{\alpha M_{PPA}}{T_{PPA}}. \quad (4)$$

Finally, the total SSA radiance is estimated to be

$$T_{SSA} = \frac{S_{SSA}}{1 - \beta}, \quad (5)$$

where S_{SSA} is the SSA single scattering radiance which can be evaluated very quickly.

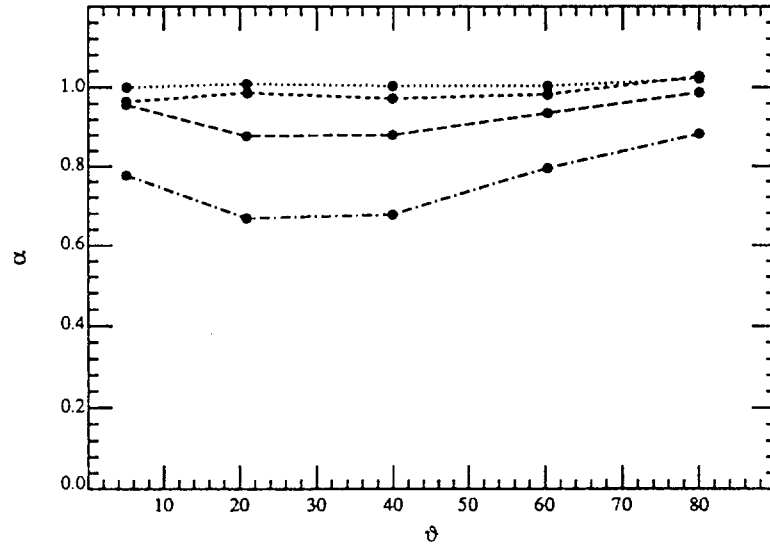


Figure 5. The α parameter vs. θ ($\phi = 90^\circ$) at $\theta_0 = 40^\circ$ is shown for different SeaWiFS bands. The curves from top to bottom refer to $\lambda = 412, 550, 670$ and 865 nm.

We applied the above scheme for several SeaWiFS bands and a few selected solar and viewing angles. The results given in Tables 2 and 3 are for the 412 and 865 nm bands. For each band, the α parameters are evaluated at $\theta_0 = 40^\circ$, $\phi = 90^\circ$, and $\theta = 5.01^\circ$, 20.9° , 39.9° and 60.3° (chosen because PPA computations are provided only at Gaussian quadrature points from a successive order of scattering solution to the radiative transfer equation), and are then applied to different θ_0 's. The SSA total radiances were calculated using the Monte Carlo simulations, and compared to the estimates using the above scheme. In the tables, "PPA" is the relative error of estimation from directly replacing the SSA radiance by its PPA counterpart, "A&K" from assuming that the conclusion of Adams and Kattawar about the ratio of single scattering to total scattering holds for all SeaWiFS bands, and "D&G" from using the procedure described above. The last column gives the differences between the Monte Carlo simulated reflectance and the estimate using our method, in terms of the SeaWiFS digital counts, or DC, the quantization interval of the sensor. For the SeaWiFS sensor, one DC is equal to $\rho_{max}/1024$, where ρ_{max} is the saturation reflectance for the respective band and 1024 is the total number of quantization intervals. It can be seen that the differences were usually less than or sometimes about one DC for our method compared to several DC's in some geometries for the other two methods.

Table 2: Errors in estimating the SSA total Rayleigh radiance with $\lambda = 412$ nm and $\phi = 90^\circ$.

θ_0 (deg.)	θ (deg.)	PPA (%)	A&K (%)	D&G (%)	D&G (DC)
60	5.01	-0.11	-0.02	-0.02	-0.08
	20.9	-0.28	-0.18	0.33	1.10
	39.9	-0.18	-0.02	0.23	0.88
	60.3	-0.41	0.02	0.27	1.48
80	5.01	-2.40	-0.11	-0.12	-0.06
	20.9	-2.62	-0.35	0.25	1.47
	39.9	-2.42	-0.13	0.14	0.95
	60.3	-2.59	-0.19	0.07	0.67

We envisage utilizing this technique in the following manner. First, from tables for ρ_r derived using a PPA code (including polarization) the value of T_{PPA} is determined. Next, S_{PPA} is computed directly, yielding M_{PPA} . Finally, coarse resolution tables of $\alpha(\theta, \phi)$ for $\theta_0 = 40^\circ$ are used to estimate β [Eq. (4)] and then Eq. (5) used to generate the final result. Since the PPA tables of ρ_r must be

Table 3: Errors in estimating the SSA total Rayleigh radiance with $\lambda = 865$ nm and $\phi = 90^\circ$.

θ_0 (deg.)	θ (deg.)	PPA (%)	A&K (%)	D&G (%)	D&G (DC)
60	5.01	0.91	0.88	-0.23	-0.14
	20.9	1.63	1.63	-0.13	-0.09
	39.9	1.94	2.01	0.04	0.03
	60.3	1.22	1.76	0.24	0.27
80	5.01	1.76	1.16	-0.34	-0.62
	20.9	2.45	1.86	0.46	-0.89
	39.9	2.69	2.15	-0.33	-0.77
	60.3	1.90	1.81	-0.10	-0.36

resident on any processing system designed for SeaWiFS imagery, the only additional requirements are the coarse resolution tables of $\alpha(\theta, \phi)$ and the computation of S_{SSA} . Note, that the PPA-computed values of ρ_r can be used for $\theta_0 \leq 70^\circ$.

Conclusions

The results presented here suggest that the effects of the curvature of the earth on the atmospheric correction of SeaWiFS (and ocean color imagery in general) appear to be negligible for solar zenith angles $\leq 70^\circ$. Furthermore, for $\theta_0 > 70^\circ$ the error in atmospheric correction can usually be reduced by computing ρ_r for a spherical-shell atmosphere. Also, for $\theta_0 > 70^\circ$ the error can be predicted reasonably well from computations made with plane-parallel atmosphere radiative transfer codes, as long as the molecular scattering component ρ_r is computed assuming a spherical-shell atmosphere. This implies that studies aimed at improving atmospheric correction can be made assuming plane-parallel geometry, and that the investigator can be confident when $\theta_0 > 70^\circ$ the results will still be valid as long as ρ_r is computed in spherical-shell geometry. Finally, a scheme based on a modification of the Adams and Kattawar¹⁶ observation — that the ratio of the single-scattered radiance to the total radiance is approximately the same for spherical-shell and plane-parallel atmospheres — is presented for deriving ρ_r for a spherical-shell atmosphere in a simple manner.

Appendix

To compare the SSA results with those of the PPA model, it is necessary to transform the angles in the spherical-shell coordinate system (the absolute frame) to those in the plane-parallel coordinate system (the local frame) placed tangent to the earth at the viewed position. In the absolute frame, the z -axis points from the origin of the earth to the sensor position in the space, the x -axis points in the projection of the incident solar beam on the plane perpendicular to the z -axis and the y -axis is defined accordingly (Figure 6). In the local frame the z' -axis points in the radial direction of the point viewed by the sensor on the outer surface of the atmosphere and the x' -axis is defined by the projection of the incident solar beam on the plane perpendicular to the z' -axis (Figure 7).

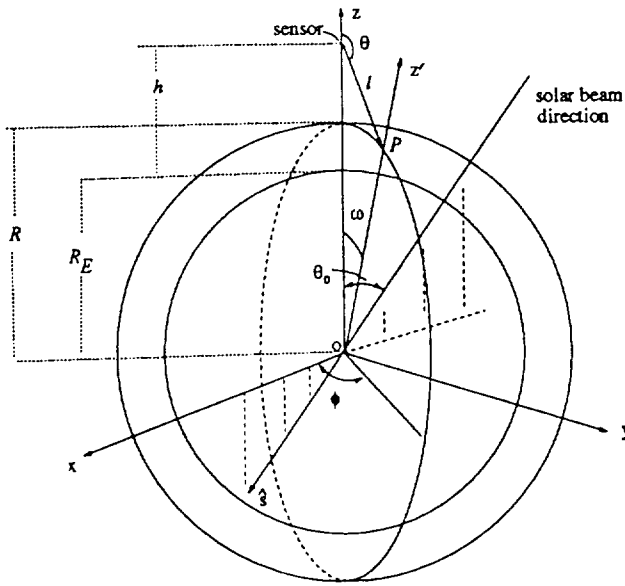


Figure 6. Geometry in the absolute frame.

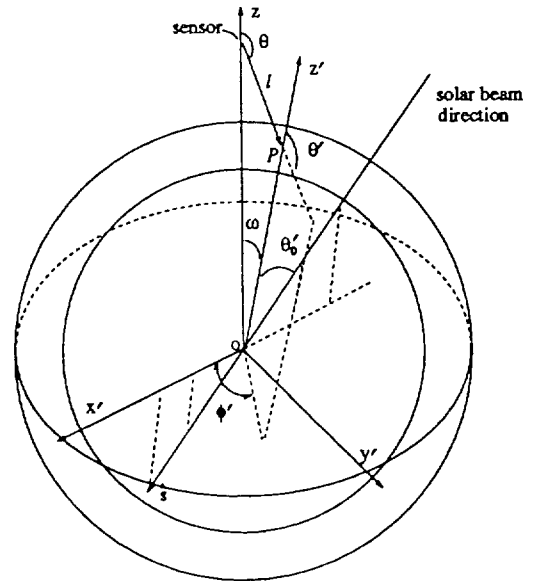


Figure 7. Geometry in the local frame.

Let θ_0 be the solar angle, then the direction vector of the solar beam in the absolute frame is

$$\hat{s} = (\sin \theta_0, 0, \cos \theta_0). \quad (6)$$

Let θ and ϕ be the viewing angles (polar and azimuthal, respectively) of the sensor, then the viewing vector in the absolute frame can be written as

$$\hat{\mathbf{v}} = (\sin \theta \cos \phi, \sin \theta \sin \phi, \cos \theta). \quad (7)$$

Given h (the satellite height), R_E (the radius of the earth), R (the distance from the origin of the earth to the local point P on the outer surface of the atmosphere) and the viewing angle θ (the angle between the local radial direction and the z -axis), ω can be easily found from

$$\cos \omega = \frac{(R_E + h) + l \cos \theta}{R},$$

where l , the distance from the sensor to the local point, is given by

$$l = -(R_E + h) \cos \theta - \sqrt{R^2 + (R_E + h)^2 (\cos^2 \theta - 1)}.$$

The representation of the z' -axis in the absolute frame is

$$\hat{\mathbf{z}}' = (\sin \omega \cos \phi, \sin \omega \sin \phi, \cos \omega).$$

Therefore, the solar angle in the local frame, θ'_0 , can be determined from

$$\cos \theta'_0 = \hat{\mathbf{s}} \cdot \hat{\mathbf{z}}' = \sin \theta_0 \sin \omega \cos \phi + \cos \theta_0 \cos \omega. \quad (8)$$

The y' -axis is formed by

$$\hat{\mathbf{y}}' = \frac{\hat{\mathbf{z}}' \times \hat{\mathbf{s}}}{|\hat{\mathbf{z}}' \times \hat{\mathbf{s}}|},$$

which in the absolute frame becomes

$$\begin{aligned} \hat{\mathbf{y}}' = \frac{1}{\sin \theta'_0} & \left[(\cos \theta_0 \sin \omega \sin \phi) \hat{\mathbf{x}} + (\sin \theta_0 \cos \omega - \cos \theta_0 \sin \omega \cos \phi) \hat{\mathbf{y}} \right. \\ & \left. + (-\sin \theta_0 \sin \omega \sin \phi) \hat{\mathbf{z}} \right]. \end{aligned} \quad (9)$$

The unit direction vector of the x' -axis is then obtained to be

$$\begin{aligned} \hat{\mathbf{x}}' &= \hat{\mathbf{y}}' \times \hat{\mathbf{z}}' \\ &= \frac{1}{\sin \theta'_0} \left\{ [\cos \omega (\sin \theta_0 \cos \omega - \cos \theta_0 \sin \omega \cos \phi) + \sin \theta_0 \sin \omega^2 \sin \phi^2] \hat{\mathbf{x}} \right. \\ &+ [-\sin \theta_0 \sin \omega^2 \sin \phi \cos \phi - \cos \theta_0 \sin \omega \cos \omega \sin \phi] \hat{\mathbf{y}} \\ &+ [\cos \theta_0 \sin \omega^2 \sin \phi^2 - \sin \omega \cos \phi (\sin \theta_0 \cos \omega - \cos \theta_0 \sin \omega \cos \phi)] \hat{\mathbf{z}} \left. \right\}. \end{aligned} \quad (10)$$

Let θ' be the angle between the z' -axis and the viewing direction, then we have

$$\cos \theta' = \hat{\mathbf{v}} \cdot \hat{\mathbf{z}}' = \cos(\theta - \omega) \quad (11)$$

Let ϕ' be the azimuth angle of the viewing direction in the local frame, then

$$\hat{\mathbf{v}} \cdot \hat{\mathbf{x}}' = \sin \theta' \cos \phi'$$

$$\hat{\mathbf{v}} \cdot \hat{\mathbf{y}}' = \sin \theta' \sin \phi'.$$

Combining Eq. (7), Eq. (10), Eq. (9) and the above two equations, we can write down

$$\begin{aligned} \sin \phi' &= \frac{\sin \theta_0 \sin \phi \sin(\theta - \omega)}{\sin \theta'_0 \sin \theta'} \\ \cos \phi' &= \frac{1}{\sin \theta'_0 \sin \theta'} \left[\sin \theta \cos \omega (\cos \omega \sin \theta_0 \cos \phi - \sin \omega \cos \theta_0) \right. \\ &\quad \left. + \cos \theta \sin \omega (\cos \theta_0 \sin \omega - \sin \theta_0 \cos \omega \cos \phi) \right]. \end{aligned} \quad (12)$$

From Equations (8), (11) and (12), one can convert θ_0 , θ and ϕ to their counterparts in the local frame, i.e., θ'_0 , θ' and ϕ' , respectively.

Conventionally, θ_0 and θ (as well as θ'_0 and θ') are referred to by the angles from the downward vertical. Then the relevant equations become

$$\begin{aligned} \cos \theta'_0 &= \cos \theta_0 \cos \omega - \sin \theta_0 \sin \omega \cos \phi \\ \cos \theta' &= \cos(\theta + \omega) \\ \sin \phi' &= \frac{\sin \theta_0 \sin \phi \sin(\theta + \omega)}{\sin \theta'_0 \sin \theta'} \\ \cos \phi' &= \frac{1}{\sin \theta'_0 \sin \theta'} \left[\sin \theta \cos \omega (\cos \omega \sin \theta_0 \cos \phi + \sin \omega \cos \theta_0) \right. \\ &\quad \left. + \cos \theta \sin \omega (\cos \theta_0 \sin \omega + \sin \theta_0 \cos \omega \cos \phi) \right]. \end{aligned} \quad (13)$$

where ω is determined from

$$\cos \omega = \frac{(R_E + h) - l \cos \theta}{R},$$

where l is given by

$$l = (R_E + h) \cos \theta - \sqrt{R^2 + (R_E + h)^2 (\cos^2 \theta - 1)}.$$

For a special case of $\phi = 90^\circ$, the equations are simplified to be

$$\begin{aligned}
 \cos \theta'_0 &= \cos \theta_0 \cos \omega \\
 \cos \theta' &= \cos(\theta + \omega) \\
 \sin \phi' &= \frac{\sin \theta_0 \sin(\theta + \omega)}{\sin \theta'_0 \sin \theta'} \\
 \cos \phi' &= \frac{\sin \omega \cos \theta_0 \sin(\theta + \omega)}{\sin \theta'_0 \sin \theta'}.
 \end{aligned} \tag{14}$$

These equations were used to compute the PPA results in the preparation of Figures 3a to 3f.

References

- [1] W. A. Hovis, D. K. Clark, F. Anderson, R. W. Austin, W. H. Wilson, E. T. Baker, D. Ball, H. R. Gordon, J. L. Mueller, S. Y. E. Sayed, B. Strum, R. C. Wrigley and C. S. Yentsch, "Nimbus 7 coastal zone color scanner: system description and initial imagery," *Science* **210**, 60-63 (1980).
- [2] H. R. Gordon, D. K. Clark, J. L. Mueller and W. A. Hovis, "Phytoplankton pigments derived from the Nimbus-7 CZCS: initial comparisons with surface measurements," *Science* **210**, 63-66 (1980).
- [3] H. R. Gordon and A. Y. Morel, *Remote Assessment of Ocean Color for Interpretation of Satellite Visible Imagery: A Review* (Springer-Verlag, New York, 1983), 114 pp.
- [4] T. Platt and S. Sathyendranath, "Oceanic Primary Production: Estimation by Remote Sensing at Local and Regional Scales," *Science* **241**, 1613-1620 (1988).
- [5] A. Morel and J. -M. André, "Pigment Distribution and Primary Production in the Western Mediterranean as Derived and Modeled From Coastal Zone Color Scanner Observations," *Jour. Geophys. Res.* **96C**, 12,685-12,698 (1991).
- [6] H. R. Gordon, "Removal of Atmospheric Effects from Satellite Imagery of the Oceans," *Applied Optics* **17**, 1631-1636 (1978).
- [7] H. R. Gordon, D. K. Clark, J. W. Brown, O. B. Brown, R. H. Evans and W. W. Broenkow, "Phytoplankton pigment concentrations in the Middle Atlantic Bight: comparison between ship determinations and Coastal Zone Color Scanner estimates," *Applied Optics* **22**, 20-36 (1983).

- [8] G. C. Feldman, N. Kuring, C. Ng, W. Esaias, C. R. McClain, J. Elrod, N. Maynard, D. Endres, R. Evans, J. Brown, S. Walsh, M. Carle and G. Podesta, "Ocean Color: Availability of the Global Data Set," *EOS Trans. Amer. Geophys. Union* **70**, 634–641 (1989).
- [9] S. B. Hooker, W. E. Esaias, G. C. Feldman, W. W. Gregg and C. R. McClain, *SeaWiFS Technical Report Series: Volume 1, An Overview of SeaWiFS and Ocean Color* (NASA Technical Memorandum 104566, July 1992).
- [10] V. V. Salomonson, W. L. Barnes, P. W. Maymon, H. E. Montgomery and H. Ostrow, "MODIS: Advanced Facility Instrument for Studies of the Earth as a System," *IEEE Geosci. Rem. Sens.* **27**, 145–152 (1989).
- [11] H. R. Gordon and D. J. Castaño, "The Coastal Zone Color Scanner Atmospheric Correction Algorithm: Multiple Scattering Effects," *Applied Optics* **26**, 2111–2122 (1987).
- [12] H. R. Gordon, J. W. Brown and R. H. Evans, "Exact Rayleigh Scattering Calculations for use with the Nimbus-7 Coastal Zone Color Scanner," *Applied Optics* **27**, 862–871 (1988).
- [13] H. R. Gordon and M. Wang, "Surface Roughness Considerations for Atmospheric Correction of Ocean Color Sensors. 1: The Rayleigh Scattering Component," *Applied Optics* **31**, 4247–4260 (1992).
- [14] H. R. Gordon and M. Wang, "Surface Roughness Considerations for Atmospheric Correction of Ocean Color Sensors. 2: Error in the Retrieved Water-leaving Radiance," *Applied Optics* **31**, 4261–4267 (1992).
- [15] H. R. Gordon and M. Wang, "Retrieval of water-leaving radiance and aerosol optical thickness over the oceans with SeaWiFS: A preliminary algorithm," *Applied Optics* **32**, 0000–0000 (1993).

- [16] C. N. Adams and G. W. Kattawar, "Radiative Transfer in Spherical Shell Atmospheres I. Rayleigh Scattering," *Icarus* **35**, 139–151 (1978).
- [17] D. G. Collins, W. G. Blattner, M. B. Wells and H. G. Horak, "Backward Monte Carlo Calculations of the Polarization Characteristics of the Radiation Emerging from Spherical Shell Atmospheres," *Applied Optics* **11**, 2684–2696 (1972).
- [18] H. R. Gordon, "Ship Perturbation of Irradiance Measurements at Sea 1: Monte Carlo Simulations," *Applied Optics* **23**, 4172–4182 (1985).
- [19] K. Ding, "*Radiative Transfer in Spherical Shell Atmospheres for Correction of Ocean Color Remote Sensing*," 1993, Ph.D. Dissertation, University of Miami, Coral Gables FL, 89 pp.
- [20] M. Wang, "*Atmospheric Correction of the Second Generation Ocean Color Sensors*," 1991, Ph.D. Dissertation, University of Miami, Coral Gables FL, 135 pp.
- [21] C. Cox and W. Munk, "Measurements of the Roughness of the Sea Surface from Photographs of the Sun's Glitter," *Jour. Opt. Soc. of Am.* **44**, 838–850 (1954).
- [22] E. P. Shettle and R. W. Fenn, *Models for the Aerosols of the Lower Atmosphere and the Effects of Humidity Variations on Their Optical Properties* (Air Force Geophysics Laboratory, Hanscomb AFB, MA 01731, AFGL-TR-79-0214, 1979).
- [23] F. X. Kenizys, E. P. Shettle, W. O. Gallery, J.H.Chetwynd, L. W. Abreu, J. E. A. Selby, S. A. Clough and R. W. Fenn, *Atmospheric Transmittance/Radiance: The LOWTRAN 6 Model* (Air Force Geophysics Laboratory, Hanscomb AFB, MA 01731, AFGL-TR-83-0187, 1983) NTIS AD A137796.
- [24] P. J. Reddy, F. W. Kreiner, J. J. Deluisi and Y. Kim, "Aerosol Optical Depths Over the Atlantic Derived From Shipboard Sunphotometer Observations During the 1988 Global Change Expedition," *Global Biogeochemical Cycles* **4**, 225–240 (1990).

- [25] K. M. Case, “Transfer Problems and the Reciprocity Principle,” *Rev. Mod. Phys.* **29**, 651–663 (1957).